

Onset of internal transport barriers in tokamaks

Cite as: Phys. Plasmas **28**, 082305 (2021); doi: 10.1063/5.0056428

Submitted: 10 May 2021 · Accepted: 29 July 2021 ·

Published Online: 16 August 2021



View Online



Export Citation



CrossMark

L. A. Osorio,¹  M. Roberto,^{2,a)}  I. L. Caldas,¹  R. L. Viana,³  and Y. Elsken⁴ 

AFFILIATIONS

¹Instituto de Física, Universidade de São Paulo, São Paulo, SP 05315-970, Brazil

²Departamento de Física, Instituto Tecnológico da Aeronáutica, São José dos Campos, SP 1228-900, Brazil

³Departamento de Física, Universidade Federal do Paraná, Curitiba, PR 81531-990, Brazil

⁴Aix-Marseille University, UMR 7345 CNRS, PIIM, Campus Saint-Jérôme, Case 322, av. esc. Normandie-Niemen, 52, FR-13397 Marseille cedex 13, France

^{a)} Author to whom correspondence should be addressed: r.marisa@gmail.com

ABSTRACT

Barriers have been identified in magnetically confined plasmas by reducing the particle transport and improving the confinement. One of them, the primary shearless barriers, is associated with extrema of non-monotonic plasma profiles. Previously, we identified these barriers in a model described by a map that allows the integration of charged particles motion in drift waves for a long timescale. In this work, we show how the existence of these robust barriers depends on the fluctuation amplitude and on the electric shear. Moreover, we also find control parameter intervals for which these primary barriers onset and breakup are recurrent. Another noticeable feature, in these transitions, is the appearance of a layer of particle trajectory stickiness after the shearless barrier breakup or before its onset. In addition to the mentioned primary barriers, we also observe sequences of secondary shearless barriers, not reported before, created and destroyed by a sequence of bifurcations as the main control parameters, the fluctuation amplitude and electric shear, are varied. Furthermore, in these bifurcations, we also find hitherto unknown double and triple secondary shearless barriers that constitute a noticeable obstacle to the chaotic transport.

Published under an exclusive license by AIP Publishing. <https://doi.org/10.1063/5.0056428>

I. INTRODUCTION

One of the questions of paramount importance in the quest for magnetically confined fusion plasmas is the understanding and control of radial particle transport.^{1–5} In particular, in order to build a future tokamak-based fusion reactor, it is mandatory to improve the energy confinement by reducing particle transport to acceptable levels.⁴

Auxiliary heating applied to tokamak discharges often leads to low confinement (L-mode) plasma regimes, for which there is an enhanced radial cross field transport due to a high level of turbulence.^{5,6} By combining neutral beam heating and a divertor, it was possible to obtain a high confinement regime (H-mode) for tokamak plasmas, with reduced transport fluxes.^{7–9}

In the latter, there is a relatively high pedestal pressure profile in the plasma column, and a large pressure gradient at the plasma edge. This increased gradient is related to a local reduction of the turbulence levels due to $\mathbf{E} \times \mathbf{B}$ shear.¹⁰ The edge transport barriers (ETBs) that are present in the H-mode can also exist inside the plasma core and are called generally internal transport barriers (ITBs), which are regions of reduced radial particle transport.² On both cases, the barriers are characterized by steep pressure gradients, however.

Another type of internal transport barrier has been recently proposed, the so-called shearless transport barriers (STBs), for which the pressure gradients are not necessarily high as in ITBs. The basic mechanism underlying the STBs is the existence of non-monotonic equilibrium radial profiles inside the tokamak. These profiles can be created by modifications of the plasma current profile and/or the application of radial electric fields.¹¹

An example of vanishing magnetic shear occurs for tokamak plasmas with a non-monotonic safety factor $q(r)$ profile, so that there can be one or more radial positions that are extremum points of $q(r)$.^{12–14} Particle transport is reduced for this type of non-monotonic discharges. At these points, a shearless toroidal magnetic surface is formed.¹⁵ Given an external perturbation with modes resonant with the magnetic surfaces in both sides of the shearless torus, twin resonant island chains are formed therein, which produce a local region of chaotic magnetic field lines attached to the islands' boundaries.^{16,17}

In a first approximation, plasma particles follow magnetic field lines that lie on magnetic surfaces, in such a way that there is no cross field transport. Within this picture, the tori surrounding the shearless curve acts as dikes preventing chaotic transport. If we consider

higher-order effects like finite Larmor-radius and collisions, there would be a transport even in the presence of magnetic surfaces.

As the perturbation intensity increases, the width of these chaotic layers is also increased, engulfing other tori between the islands and the shearless torus. Increasing further the perturbation, all the tori can be destroyed, and, even after the shearless torus is broken, it still acts as a transport barrier. This occurs because of a dynamical effect called stickiness, which makes a chaotic trajectory to wander erratically in the vicinity of the torus remnant, yielding trajectories with large escape times, so reducing effectively the transport fluxes.¹⁸

There are other sources of vanishing shear that can be related to the formation of shearless transport barriers. The introduction of a bias electrode in the plasma column produces a radial electric field that improves plasma confinement in tokamaks.¹⁹ In particular, a decrease was observed in the levels of the low-frequency component of the fluctuating floating potential as well as the turbulent-driven particle flux.²⁰ The production of shearless transport barriers due to a non-monotonic radial electric field produced by polarizing the tokamak vessel has been numerically investigated by considering a drift-kinetic model for particle transport driven by drift waves.^{21–23}

A further physical mechanism that can also trigger the formation of shearless transport barriers is the presence of non-monotonic plasma toroidal velocity profiles.²⁴ The existence of such barriers has been observed in the Texas Helimak, where a set of diagnostic probes is mounted to measure plasma flow velocity in various points, so that velocity shears can be detected in the discharges.^{25,26}

We have applied the model introduced in Ref. 22 to predict numerically the existence of STBs in tokamak discharges with non-monotonic plasma profiles.^{21,27,28} In this paper, our main goal is to examine in detail the onset of shearless transport barriers in tokamaks associated with one of those described sources of non-monotonic plasma profiles, namely, the radial electric field. The common framework to deal with these physical mechanisms is the drift-kinetic model of Ref. 22, where we describe guiding center motion of plasma particles under $\mathbf{E} \times \mathbf{B}$ drift with contributions of the parallel velocity v_{\parallel} as well. The equations of motion are numerically integrated, and Poincaré maps are obtained for discrete times.

Since the ensuing dynamical model is non-integrable, we typically observe chaotic motion related to the resonant boundaries. From the numerically obtained Poincaré maps, we are able to detect the formation of shearless transport barriers. We call these barriers as primary because they can be associated with the non-monotonic equilibrium profile and the corresponding extrema of the rotation number profile.

Using the drift-kinetic model, we investigate the behavior of the primary shear transport barriers when model parameters are changed, particularly how they depend on the amplitude of electrostatic fluctuations and the extremum of radial electric field. We show the barriers breakup and resurge, recurrently, as those parameters are varied. In these transitions, after the shearless barrier breakup or before its onset, we also find the appearance of a layer of particle trajectory stickiness, which is an obstruction to chaotic transport.

In addition to the mentioned primary barriers, we also find secondary shearless barriers recurrently, created and destroyed by a sequence of bifurcations that create new extrema in the rotation number profile. Furthermore, in these bifurcations, we also find hitherto

unknown double and triple secondary shearless barriers that also constitute a noticeable obstacle to the chaotic transport.

The paper is organized as follows. Sec. II introduces the drift-kinetic model and the non-monotonic plasma profiles used in numerical simulations. Section III discusses the influence of the fluctuation amplitude on the shearless transport barriers. The formation of effective barriers due to stickiness effect, after the shearless curve has been destroyed, is discussed in Sec. IV. The influence of the radial electric field profile on the formation of shearless barriers is the subject of Sec. V. The Sec. VI is devoted to our Conclusions.

II. DRIFT WAVE MODEL

The chosen drift wave model introduces the basic equations of motion to describe the trajectories of particles along magnetic field lines and electrical drifts. We consider an electrostatic equilibrium field in the radial direction and drift waves that propagate in the poloidal and toroidal directions. These drift waves arise from non-uniformity at the plasma edge and are analyzed in the toroidal section of magnetic confinement in the tokamak.^{1,22,27–30} Fluctuations in electrostatic potential are written as a function of amplitude, and in spatial and temporal modes.^{27,28}

The trajectories of the particles are described by the movement of the guiding center,

$$\frac{d\mathbf{x}}{dt} = v_{\parallel} \frac{\mathbf{B}}{B} + \frac{\mathbf{E} \times \mathbf{B}}{B^2}. \quad (1)$$

We consider, initially, that the components of this equation are given in local polar coordinates $\mathbf{x} = (r, \theta, \varphi)$.

This plasma configuration corresponds to a cylindrical approximation of a toroidal section of a tokamak of high aspect ratio ($a/R \simeq 0.3$), where a and R are, respectively, the minor and major plasma radii. For the field components, we assume a magnetic configuration with $B \approx B_{\varphi} \gg B_{\theta}$ and the safety factor given by $q(r) = \frac{rB_{\varphi}}{RB_{\theta}}$. The electric field consists of an equilibrium part with intensity given by E_r , defined by a radial profile, and a floating part, so that $\tilde{\mathbf{E}} = -\nabla\tilde{\phi}$. Therefore, this model allows to investigate the simultaneous influence of the electric shear, due to the spatial variations of the electric field, and the magnetic shear, when considering the spatial variations of the safety factor, in the chaotic transport at the plasma edge.

We follow the procedure adopted in Ref. 22, writing the equations in the action variable $I \equiv (r/a)^2$ and angle variable $\psi \equiv M\theta - L\varphi$. Poloidal and toroidal spatial modes are defined, respectively, by the wave numbers M and L . In this way, we assume coherent oscillations, where ψ represents a helical angle defined by dominant modes. When considering these new variable components of the guiding center, we obtain

$$\frac{dI}{dt} = 2M \sum_n \phi_n \sin(\psi - n\omega_0 t + \alpha_n), \quad (2)$$

$$\frac{d\psi}{dt} = \frac{a}{R} v_{\parallel}(I) \frac{[M - Lq(I)]}{q(I)} - \frac{M}{\sqrt{I}} E_r(I), \quad (3)$$

where a normalization with the characteristic magnitude scales a , B , and E_0 was done. Note that all the plasma profiles are defined as functions of the action variable. For the floating potential, we use a finite mode drift wave spectrum,

$$\tilde{\phi}(\mathbf{r}, t) = \sum_n \phi_n \cos(\psi - n\omega_0 t + \alpha_n), \quad (4)$$

where ϕ_n is the perturbed amplitude, ω_0 is the lowest angular frequency of the drift wave spectrum, and α_n are constant phases that do not affect the resonant conditions. Temporal modes are defined by the wave numbers n . Thus, we can assume one or more drift waves that describe fluctuations in the electrostatic potential of the model.

In Sec. III, for numerical applications, we introduce typical parallel speed and radial electric field profiles experimentally measured in the TCABR tokamak.³⁰ We also assume a monotonic safety factor profile commonly observed in tokamaks.⁴ The resonance conditions are determined by the combination of the safety factor, parallel plasma velocity, and electric field profiles. Thus, taking $\frac{d}{dt}(\psi - n\omega_0 t - \alpha_n) = 0$, we obtain the primary resonance condition. Furthermore, we also show the Poincaré maps by integrating Eqs. (2) and (3) for various initial conditions chosen to clearly represent the most important islands, invariant lines, and the chaotic region. The intersections of the integrated trajectories are selected at the toroidal section corresponding to instants $t_j = j2\pi/\omega_0$ ($j = 0, 1, 2, \dots$). In Poincaré maps, the minor plasma radius lies at $I = 1.0$, but we consider I up to 1.4 to investigate the particle transport to the chamber wall.

III. INFLUENCE OF THE FLUCTUATION AMPLITUDE ON THE SHEARLESS TRANSPORT BARRIERS

According to Eq. (2), for null perturbing amplitudes, $\phi_n = 0$, the system is integrable; it means that each trajectory is periodic or quasi-periodic and stays in invariant lines in the Poincaré map with the initial action $I_0 = \text{constant}$. When $\phi_n \neq 0$, we have chaotic trajectories and regular invariant lines, and we can use the rotation number, defined as $\Omega = \lim_{i \rightarrow \infty} (\psi_i - \psi_0)/i$, where ψ_i refers to the i th section to analyze the behavior of the invariant lines in the phase space. The rotation number profile is determined for initial conditions with a fixed angle ψ_0 for several values of action variable I . Although other choices of ψ_0 would result in different profiles, the identified islands and other invariants would be essentially the same. This happens because each invariant and island depend on both variables ψ and I , but are labeled by a unique identifying rotation number. If $d\Omega/dI = 0$, the profile has an extremum at (I, ψ_0) . This point is part of a shearless invariant curve, which acts as a barrier separating the particle orbits in the phase space and reducing the particle transport. These are the primary shearless invariant curves if their origin can be associated with the rotation number extrema obtained from the equilibrium plasma profiles. However, in this work, we also present secondary shearless invariant curves that are due to bifurcations that create new rotation number extrema for varying control parameters.

In order to solve our numerical model, we use the parallel velocity and radial electric field profiles, with $a = 0.18$ m, $B = 1.1$ T, and $E_0 = 4.6$ kV/m, as given in Ref. 21, which are similar to those observed in TCABR tokamak.³⁰ The velocity profile is given by Eq. (5), which fits with experimental TCABR data points, as described in Ref. 21. The equilibrium radial field E_r is written in Eq. (6), with $\alpha = -0.563$, $\beta = 1.250$, and $\gamma = -1.304$. Furthermore, we assume the safety factor profile as Eq. (7), a common approximation for large aspect ratio tokamaks,

$$v_{\parallel}(r) = -1.43 + 2.82 \tanh\left(20.3 \frac{r}{a} - 16.42\right), \quad (5)$$

$$E_r(r) = 3\alpha \left(\frac{r}{a}\right)^2 + 2\beta \frac{r}{a} + \gamma, \quad (6)$$

$$q(r) = 1.0 + 3.0 \left(\frac{r}{a}\right)^2. \quad (7)$$

Applying the resonant condition for the chosen radial profiles, we verify that the resonant modes are $n = 3$ and $n = 4$. We select from the spectrum analysis, a frequency around 62.1 kHz, which gives $\omega_0 = 2.673$. The perturbing electric potential amplitudes ϕ_n are normalized by aE_0 . We consider spatial wave numbers $M = 16$ and $L = 4$, chosen as typical numbers in the tokamak wave spectrum at plasma edge.²²

In order to analyze the influence of the fluctuation amplitudes on the shearless barriers, we keep fixed the perturbation amplitudes $\phi_3 = 1.0 \times 10^{-3}$ and $\phi_4 = 0.12 \times 10^{-3}$ and vary the non-resonant mode ϕ_2 . We keep constant all the parameters of the equilibrium profiles. The objective is to investigate the recurrent breakup and onset of the barriers as the fluctuation amplitude is varied. Following that, Fig. 1 shows the Poincaré maps for $\phi_2 = 0, 1.5 \times 10^{-3}, 1.6 \times 10^{-3}$, and 1.8×10^{-3} . The barrier already exists for a null $n = 2$ amplitude, breaks up for the perturbing amplitude $\phi_2 = 1.6 \times 10^{-3}$, and resurges for $\phi_2 = 1.8 \times 10^{-3}$. So, we see that the existence of the barrier is sensitive to small variations in the fluctuation amplitude, a characteristic that will be explored in this section.

To confirm the existence of the shearless curve, we present, in Fig. 2, the magnified rotation number profiles for Figs. 1(b) and 1(d), calculated for initial conditions at $\psi = 0$, with local I maxima. The I maxima and the angle $\psi = 0$ are used as initial coordinates and iterated to trace in red the shearless curves shown in Figs. 1(b) and 1(d).

Next, for increasing values of ϕ_2 , we observe a sequence of shearless curve break-ups in phase space. Figure 3 shows three shearless curves for $\phi_2 = 6.8 \times 10^{-3}$, two shearless curves for $\phi_2 = 6.9 \times 10^{-3}$, one shearless curve for $\phi_2 = 7.1 \times 10^{-3}$, and no shearless curve for $\phi_2 = 7.5 \times 10^{-3}$ with a stickiness region left by the previous barrier. This kind of bifurcation has been observed in theoretical non-twist dynamical systems³¹ and, in the context of this article, represents a reinforcement of barriers attenuating the particle transport.

For each colored STB seen in Fig. 3, we present, in Fig. 4, the associated magnified rotation number profiles in the same color as the STB curves, calculated in the non-chaotic map region, for initial conditions with $\psi = 0$. These STBs can be generated by the initial coordinates $\psi = 0$ and I corresponding to the local maxima indicated in the profiles of Fig. 4.

To show that the existence of barriers depends on the fluctuation amplitude ϕ_2 , we check their existence in an interval of ϕ_2 from 0 to 8.5×10^{-3} , with a step 0.1×10^{-3} . The results are shown in Fig. 5. In this figure, the red, blue, and green bars represent the amplitude range for which barriers exist; otherwise, we draw a black bar when the barrier is not observed. We also present magnifications to better show the shearless bifurcations changing the number of barriers. Figure 5(a) shows the rotation number as a function of fluctuation amplitude, and Fig. 5(b) shows the shearless barrier position as a function of ϕ_2 . We conclude that as the amplitude of the fluctuation varies, the shearless barriers can be recurrently destroyed and restored. It means that the existence of barriers, in tokamak discharges, may depend on the fluctuation amplitude. In addition, for some fluctuation ranges, there are

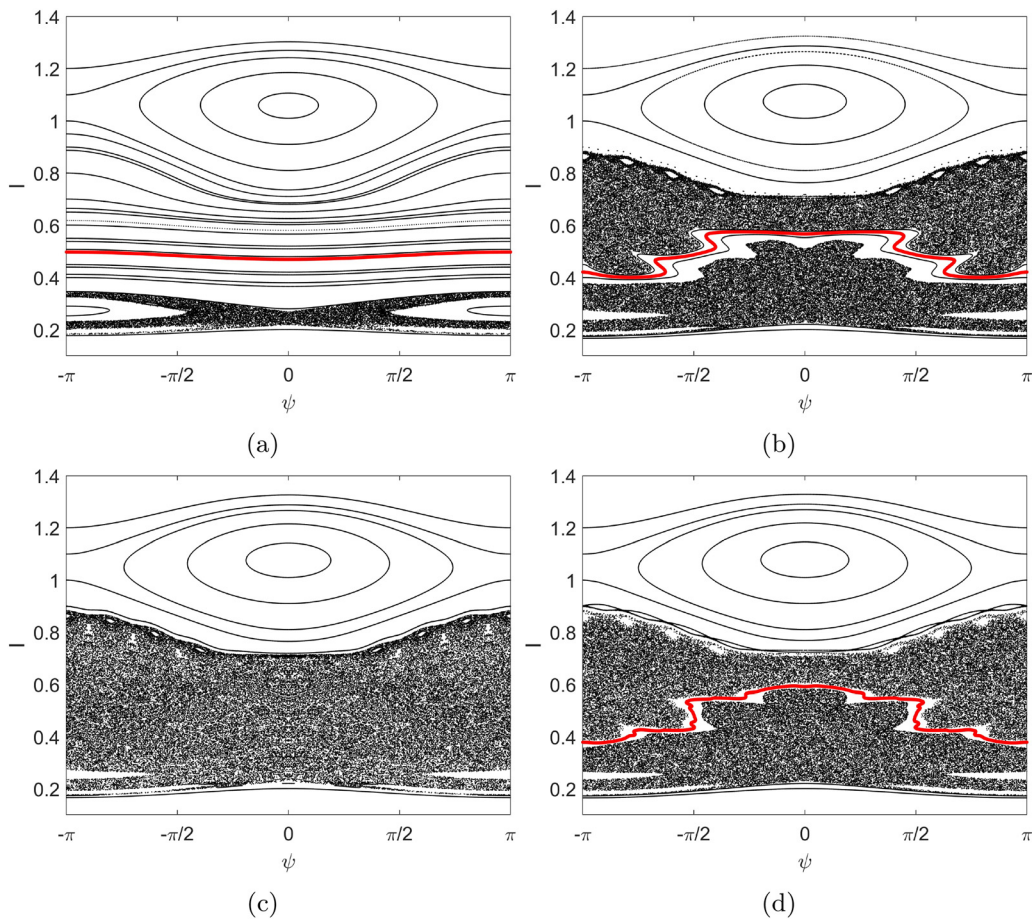


FIG. 1. Poincaré maps for (a) $\phi_2 = 0$, (b) $\phi_2 = 1.5 \times 10^{-3}$, (c) 1.6×10^{-3} , and (d) 1.8×10^{-3} . The shearless curve, marked in red, disappears for $\phi_2 = 1.6 \times 10^{-3}$ and resurges for $\phi_2 = 1.8 \times 10^{-3}$.

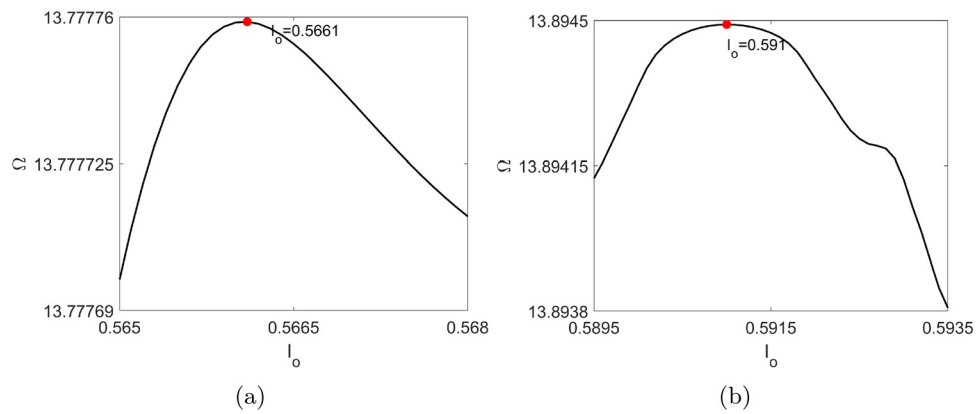


FIG. 2. Rotation number profiles to (a) $\phi_2 = 1.5 \times 10^{-3}$ and (b) 1.8×10^{-3} for a set of initial conditions I_0 . The red dots correspond to shearless actions, indicated in the figures, required to obtain the shearless curves of Figs. 1(b) and 1(d).

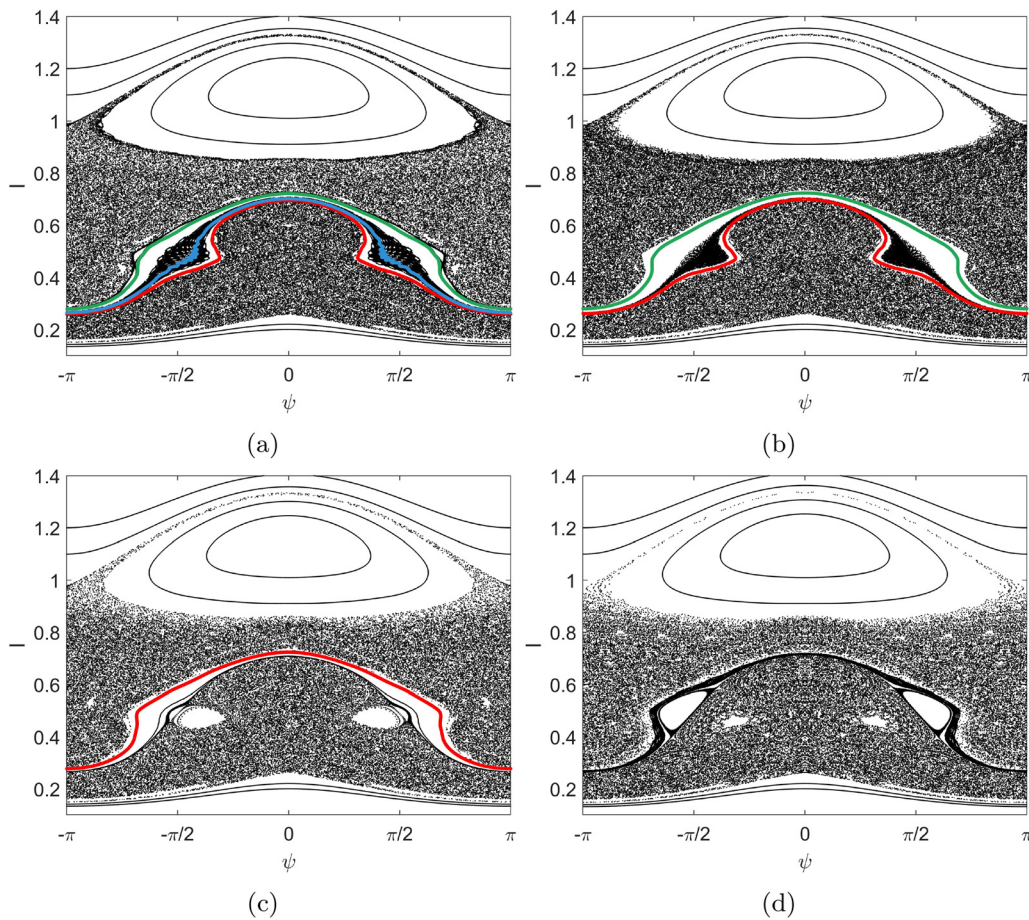


FIG. 3. Three shearless curves, marked in red, blue, and green, for (a) $\phi_2 = 6.8 \times 10^{-3}$. (b) Break-up of a shearless curve with two remaining shearless curves, marked in red and green, for $\phi_2 = 6.9 \times 10^{-3}$. (c) One remaining shearless curve, marked in red, for $\phi_2 = 7.1 \times 10^{-3}$. (d) No shearless curve for $\phi_2 = 7.5 \times 10^{-3}$.

barrier bifurcations giving rise to a second and, possibly, a third barrier.

IV. PERSISTENT BARRIERS

A noticeable feature in non-twist systems is the appearance of a layer of stickiness after the shearless barrier breakup or before its onset.³² A stickiness layer separates the chaotic region in two parts, and, to cross this layer, orbits get trapped for a high number of iterations.³³ Accordingly, for some domains of the amplitude perturbation, in the present analysis, we observe that stickiness regions appear in phase space, associated with the shearless barrier breakup or to its onset. This is the case for $\phi_2 = 2.0 \times 10^{-3}$. Taking $\phi_2 = 2.1 \times 10^{-3}$, the barrier is destroyed and a stickiness region is magnified, as shown in Fig. 6, separating the chaotic orbits around the stickiness layer.

In Fig. 6(b), one chaotic orbit in blue and another one in black fill separated areas in phase space, with a high concentration of iterations in the stickiness region, spending a long time to cross this region. The possible crossings are too long to be observed in Fig. 6(b). Thus, even if the barrier is broken up, there is a long stickiness inhibiting the particle transport in this region, indicating the persistence of barrier effect, even after the barrier disappearance.

Figure 7 shows the emergence of stickiness, precursor of the shearless curve, for $\phi_2 = 5.6 \times 10^{-3}$. For $\phi_2 = 5.7 \times 10^{-3}$, the shearless curve onset occurs in the stickiness layer. This transformation is the reverse sequence of that shown in Fig. 6, namely, the stickiness appears before the barrier onset and not after its destruction. It also indicates the persistence of the barrier effect after this disappearance for decreasing fluctuation amplitude.

As we show in Fig. 8, increasing the perturbation amplitude, for $\phi_2 = 6.6 \times 10^{-3}$, there is no shearless curve. However, for $\phi_2 = 6.61 \times 10^{-3}$, a shearless curve appears, and then, for $\phi_2 = 6.7 \times 10^{-3}$, we see two shearless curves (in blue and red). In this figure, we have an example of a large region of stickiness, with many visible islands, associated with the onset of multiple shearless barriers.

V. INFLUENCE OF THE RADIAL ELECTRIC FIELD PROFILE ON THE SHEARLESS TRANSPORT BARRIERS

The experiments show that the transport barriers appear by modifications of the radial electric field E_r in high confinement regime, as discussed in the Introduction. On the other hand, shearless barriers appear as a mechanism to prevent chaotic particle transport: even after

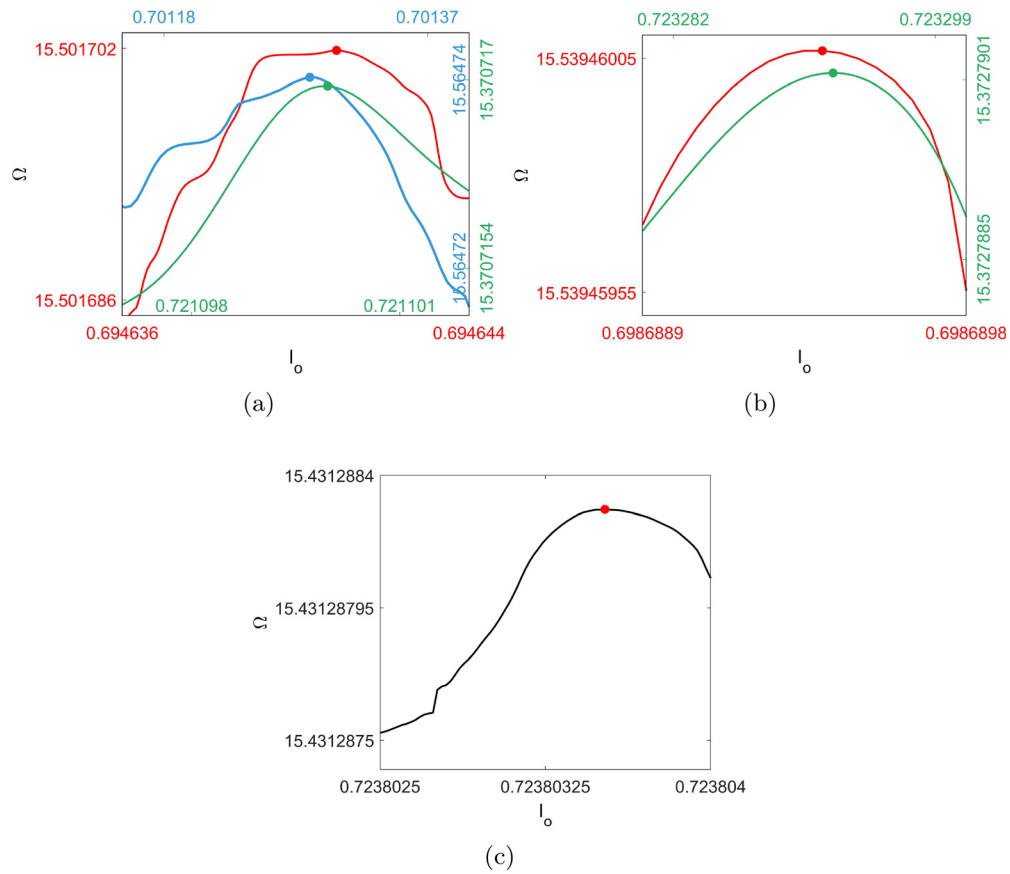


FIG. 4. Rotation number profiles for (a) $\phi_2 = 6.8 \times 10^{-3}$, (b) $\phi_2 = 6.9 \times 10^{-3}$, and (c) $\phi_2 = 7.1 \times 10^{-3}$. For each STB seen in Fig. 3, there is a rotation number profile in the same color as the barrier. Note that each profile, in red, blue, green, and black, is associated with a unique barrier and has different Ω and I_0 linear scales.

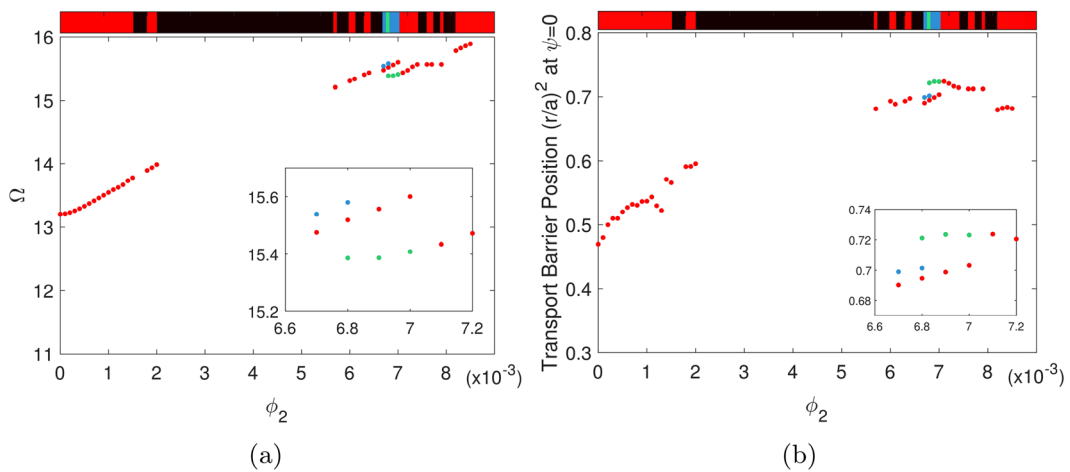


FIG. 5. (a) Rotation number Ω as function of the fluctuation amplitude ϕ_2 . Red (black) bars indicate the existence (non-existence) of shearless barriers. For some values of ϕ_2 , there are two or three shearless curves indicated in blue or green bars. (b) Transport barrier position I at $\psi = 0$ vs ϕ_2 .

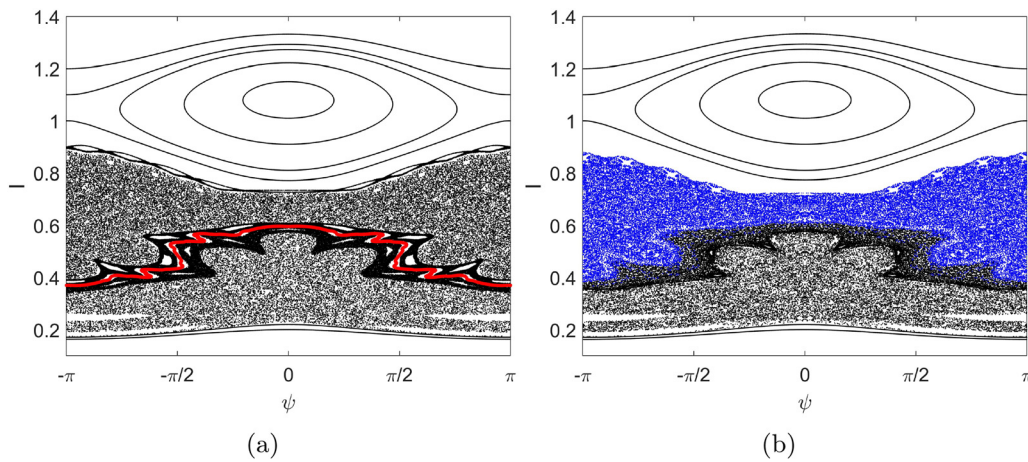


FIG. 6. (a) Shearless curve, in red color, for $\phi_2 = 2.0 \times 10^{-3}$ and the stickiness appearance around this curve. (b) For $\phi_2 = 2.1 \times 10^{-3}$, the shearless curve is destroyed and the stickiness region expanded. Two chaotic orbits in blue and black are concentrated in the stickiness region and take a long time to cross this region. The stickiness regions are identified by the high concentration of black points.

the invariant curve has been broken, the islands still remain with large stickiness that reduces the transport.

To verify the influence of the radial electric field profile on the existence of the shearless barriers, we fix the fluctuation amplitude ϕ_2 , choosing $\phi_2 = 1.6 \times 10^{-3}$, and vary the parameter k , defined as $k = -\beta/(3\alpha)$, that corresponds to the radial position of the maximum of the electric field (normalized to the plasma radius). The parameters α and β are defined in the expression of E_r introduced in Eq. (6).²¹ In Secs. III and IV, $k = 0.74$. Figures 9(a) and 9(b) show how the rotation number changes with the parameter k . In this figure, the red and blue bars indicate the parameter range for which barriers are identified, and the black bars represent the barriers absence. Figure 9(b) is a magnification of Fig. 9(a). As the radial electric field profile changes, the resonance condition also changes, and this is the reason why there is no shearless barrier in the range around $k = 0.74$, where the resonance

condition also includes $n = 2$. Figure 9 also shows an interval of parameter k for which two barriers exist.

It is also noted that in the interval $k = [0.7, 0.78]$, as shown in the top bar of Fig. 9(b), the shearless barrier appears and disappears on repeated occasions. To clarify this point, we show in Fig. 10(a) the Poincaré map for $k = 0.704$. There is no shearless barrier in this case, and only the chaotic trajectories are observed. A small modification of parameter k to $k = 0.7044$, as shown in Fig. 10(b), determines the appearance of the shearless barrier, and this scenario occurs repeatedly as the electric field profile changes, as shown in Figs. 9(a) and 9(b).

Figures 11(a) and 11(b) show the transport barrier position I , at $\psi = 0$, as a function of k for a fixed amplitude $\phi_2 = 1.6 \times 10^{-3}$. Figure 11(b) is a magnification of Fig. 11(a). Similar to the conclusions of Fig. 9, on varying the parameter k , we find that the shearless barriers are sensitive to this parameter. Thus, a small variation of k , inherent to

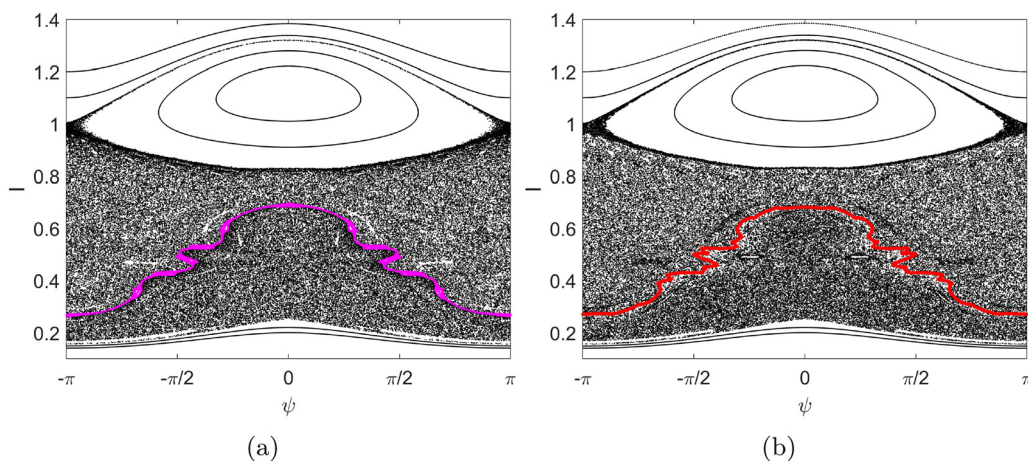


FIG. 7. (a) Emergence of stickiness, precursor of the shearless curve for $\phi_2 = 5.6 \times 10^{-3}$. The stickiness layer is represented in magenta, where the shearless curve is created. (b) Shearless curve onset in the stickiness region, for $\phi_2 = 5.7 \times 10^{-3}$, in red.

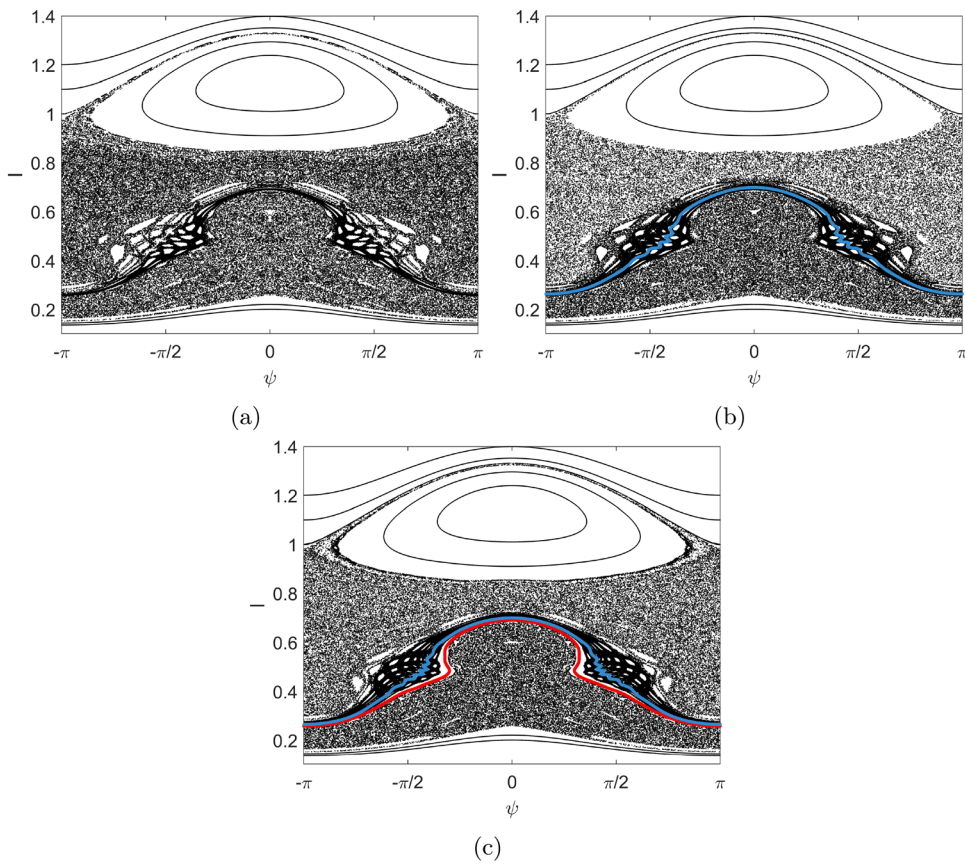


FIG. 8. (a) No shearless curve for $\phi_2 = 6.6 \times 10^{-3}$. (b) Emerging shearless curve for $\phi_2 = 6.61 \times 10^{-3}$, shown in blue. (c) Two shearless barriers for $\phi_2 = 6.7 \times 10^{-3}$, shown in red and blue.

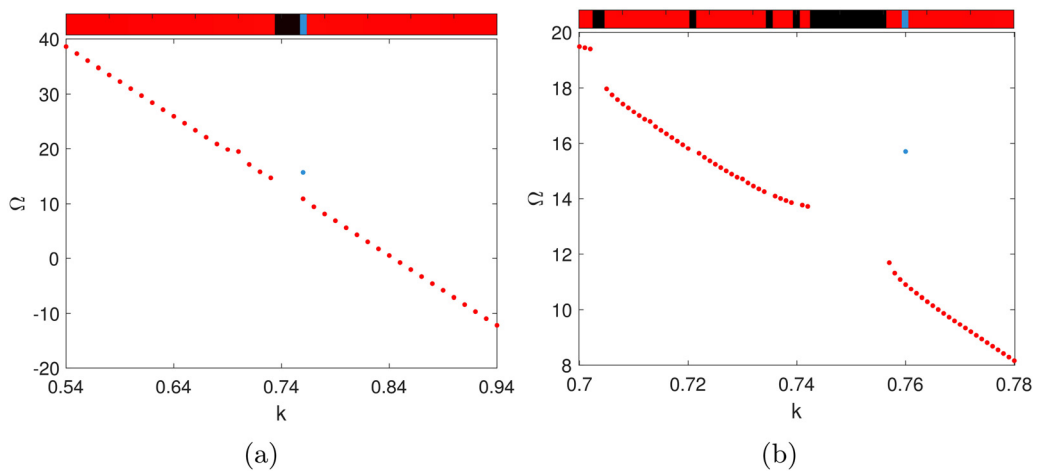


FIG. 9. Rotation number Ω as function of the parameter k . Red (black) bars indicate the existence (non-existence) of shearless barriers. The blue bar indicates an interval with two shearless barriers. (a) Ω vs k for a fixed $\phi_2 = 1.6 \times 10^{-3}$. (b) Zoom in the interval $0.7 \leq k \leq 0.78$.

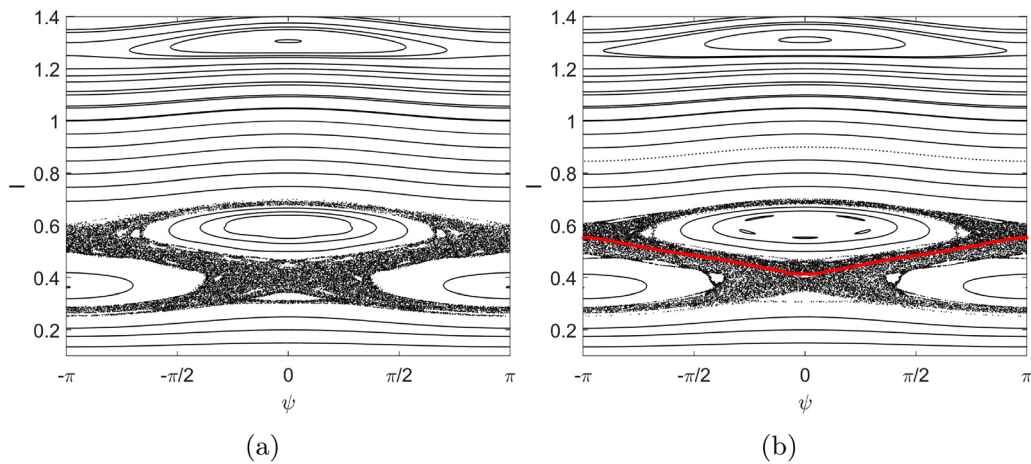


FIG. 10. (a) No shearless barrier for $k = 0.704$ and (b) sudden appearance of a shearless barrier around $k = 0.7044$, marked in red.

the plasma discharges evolution, can break or create such barriers or even move it toward the edge.

VI. CONCLUSIONS

The existence of shearless transport barriers represents a novel feature in the investigation of the possible ways to control or mitigate particle transport in tokamaks and other toroidal devices like the Texas Helimak. While internal transport barriers are usually related to strong density gradients, both in the plasma edge and its core, shearless transport barriers appear due to a different cause, namely, the existence of non-monotonic plasma profiles. These primary shearless barriers are located at the extremum points of those profiles and do not need strong density gradients to be effective against particle transport.

There are three types of non-monotonic plasma profiles that can be harnessed in order to create shearless transport barriers: (i) magnetic shear (safety factor); (ii) radial electric field; and (iii) toroidal

plasma velocity. In the present paper, we investigated the production of shearless transport barriers through the non-monotonic profile (ii), using a drift-kinetic model (the safety factor profile was kept monotonic). The numerical integration of the model equations is used to obtain a Poincaré map for canonically conjugate variables (I, ψ) .

Considering that the chaotic particle transport is influenced by a turbulent fluctuation spectrum, we considered a finite drift-wave mode spectrum for the floating electrostatic potential. The intensity of the non-resonant mode (ϕ_2) has been used as a variable control parameter. On increasing the latter, we have shown that a primary shearless transport barrier that is destroyed for a given value of ϕ_2 can reappear at a slightly larger value. The reason for this behavior is that shearless barriers occur at local extremum points of the rotation number, which is the average progress of the ψ variable per map iteration. Alterations in the value of the perturbation strength modify the rotation number radial profiles, which can either create or destroy local extrema. Moreover, for some specific intervals of the control

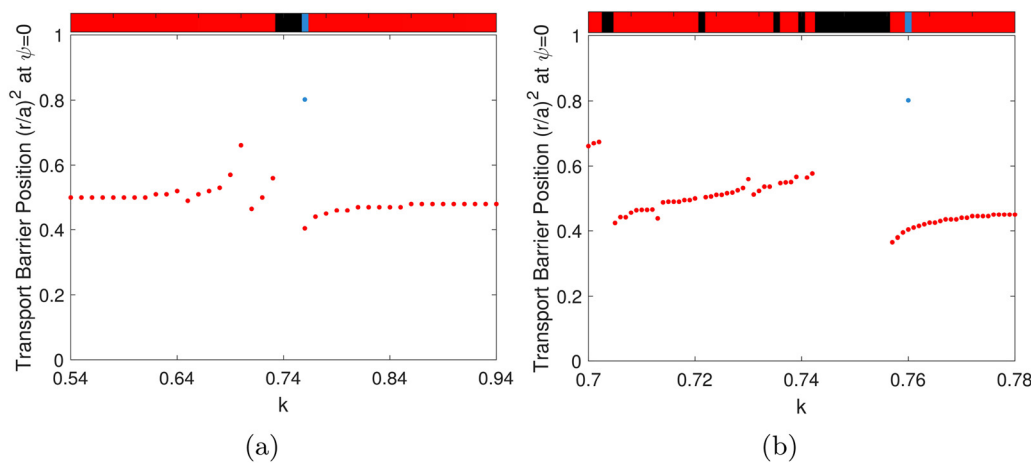


FIG. 11. (a) Transport barrier position l , at $\psi = 0$, vs k for a fixed $\phi_2 = 1.6 \times 10^{-3}$. (b) Zoom in the interval $0.7 \leq k \leq 0.78$.

parameters, we identify new sequences of secondary transport barriers not associated with the non-monotonic plasma profile. Furthermore, these secondary barriers are formed by two or three coexisting shearless invariants, constituting a noticeable obstacle to the chaotic particle transport at the plasma edge.

The shearless barriers described above are truly invariant curves of the Poincaré map of the particle trajectories. However, even after these curves are destroyed, their remnants may cause a stickiness effect that effectively traps chaotic trajectories thereby for a relatively long time. This can also be regarded as a (partial) shearless barrier. We have described those persistent barriers as the control parameter is varied.

The shearless barriers can also be investigated by altering the radial electric field profile, keeping constant the perturbation modes amplitude. This can be done in the context of our model by altering the position of the radial electric field extremum (k). As before, we can also detect the breakup and resurfing of shearless barriers as the new control parameter is varied, and regions of barrier coexistence can be also observed. These multiple barriers can be related to double or triple shearless bifurcation. The effect of a small modification of the parameter k on the appearance of barriers could be validated in experiments for time-dependent electric fields.

In conclusion, by varying the amplitude fluctuation or the electric shear, we find intervals of these control parameters for which the barriers onset and breakup are recurrent.

ACKNOWLEDGMENTS

The authors thank the financial support from the Brazilian Federal Agencies (CNPq) under Grant Nos. 407299/2018-1 and 302665/2017-0 and the São Paulo Research Foundation (FAPESP, Brazil) under Grant Nos. 2018/03211-6, 2018/14435-2, and 2020/01399-8, and support from Coordenação de Aperfeiçoamento de Pessoal de Nível Superior (CAPES) under Grant No. 88881.143103/2017-01 and Comité Français d'Evaluation de la Coopération Universitaire et Scientifique avec le Brésil (COFECUB) under Grant No. 40273QA-Ph908/18.

DATA AVAILABILITY

The data that support the findings of this study are available from the corresponding author upon reasonable request.

REFERENCES

- ¹W. Horton, *Turbulent Transport in Magnetized Plasmas*, 2nd ed. (World Scientific, 2018).
- ²R. C. Wolf, *Plasma Phys. Controlled Fusion* **45**, R1 (2002).
- ³R. D. Hazeltine and J. D. Meiss, *Plasma Confinement* (Dover, 2003).
- ⁴C. W. Horton, Jr. and S. Benkadda, *ITER Physics* (World Scientific, 2015).
- ⁵R. J. Goldston, *Plasma Phys. Controlled Fusion* **26**, 87 (1984).
- ⁶P. N. Yushmanov, T. Takizuka, K. S. Riedel, O. J. W. F. Kardaun, J. G. Cordey, S. M. Kaye, and D. E. Post, *Nucl. Fusion* **30**, 1999 (1990).
- ⁷F. Wagner, G. Becker, K. Behringer, D. Campbell, A. Eberhagen, W. Engelhardt, G. Fussmann, O. Gehre, J. Gernhardt, G. v Gierke *et al.*, *Phys. Rev. Lett.* **49**, 1408 (1982).
- ⁸J. W. Connor, T. Fukuda, X. Garbet, C. Gormezano, V. Mukhovatov, and M. Wakatani, *Nucl. Fusion* **44**, R1 (2004).
- ⁹X. Garbet, P. Mantica, C. Angioni, E. Asp, Y. Baranov, C. Bourdelle, R. Budny, F. Crisanti, G. Cordey, L. Garzotti *et al.*, *Plasma Phys. Controlled Fusion* **46**, B557 (2004).
- ¹⁰K. H. Burrell, *Phys. Plasmas* **4**, 1499 (1997).
- ¹¹I. L. Caldas, R. L. Viana, C. V. Abud, J. C. D. d Fonseca, Z. d O. Guimarães Filho, T. Kroetz, F. A. Marcus, A. B. Schelin, J. Szezech, D. L. Toufen *et al.*, *Plasma Phys. Controlled Fusion* **54**, 124035 (2012).
- ¹²F. M. Levinton, M. C. Zarnstorff, S. H. Batha, M. Bell, R. E. Bell, R. V. Budny, C. Bush, Z. Chang, E. Fredrickson, A. Janos *et al.*, *Phys. Rev. Lett.* **75**, 4417 (1995).
- ¹³E. J. Strait, L. L. Lao, M. E. Mauel, B. W. Rice, T. S. Taylor, K. H. Burrell, M.-S. Chu, E. A. Lazarus, T. H. Osborne, S. J. Thompson *et al.*, *Phys. Rev. Lett.* **75**, 4421 (1995).
- ¹⁴E. Mazzucato, S. H. Batha, M. Beer, M. Bell, R. E. Bell, R. V. Budny, C. Bush, T. S. Hahm, G. W. Hammett, F. M. Levinton *et al.*, *Phys. Rev. Lett.* **77**, 3145 (1996).
- ¹⁵P. J. Morrison, *Phys. Plasmas* **7**, 2279 (2000).
- ¹⁶D. del Castillo-Negrete and P. J. Morrison, *Phys. Fluids A* **5**, 948 (1993).
- ¹⁷D. del Castillo-Negrete, J. M. Greene, and P. J. Morrison, *Physica D* **91**, 1–23 (1996).
- ¹⁸J. D. Szezech, Jr., I. L. Caldas, S. R. Lopes, R. L. Viana, and P. J. Morrison, *Chaos* **19**, 043108 (2009).
- ¹⁹I. C. Nascimento, Y. K. Kuznetsov, J. H. F. Severo, A. M. M. Fonseca, A. Elfimov, V. Bellintani, M. Machida, M. V. A. P. Heller, R. M. O. Galvão, E. K. Sanada *et al.*, *Nucl. fusion* **45**, 796 (2005).
- ²⁰G. Van Oost, J. Adamek, V. Antoni, P. Balan, J. A. Boedo, P. Devynck, I. Duran, L. Eliseev, J. P. Gunn, M. Hron *et al.*, *Plasma Phys. Controlled Fusion* **45**, 621 (2003).
- ²¹F. A. Marcus, M. Roberto, I. L. Caldas, K. C. Rosalem, and Y. Elskens, *Phys. Plasmas* **26**, 022302 (2019).
- ²²W. Horton, H.-B. Park, J.-M. Kwon, D. Strozzi, P. Morrison, and D.-I. Choi, *Phys. Plasmas* **5**, 3910 (1998).
- ²³F. A. Marcus, I. L. Caldas, Z. O. Guimarães-Filho, P. J. Morrison, W. Horton, Y. K. Kuznetsov, and I. C. Nascimento, *Phys. Plasmas* **15**, 112304 (2008).
- ²⁴R. M. Ferro and I. L. Caldas, *Phys. Lett. A* **382**, 1014 (2018).
- ²⁵K. W. Gentle, K. Liao, K. Lee, and W. L. Rowan, *Plasma Sci. Technol.* **12**, 391 (2010).
- ²⁶D. L. Toufen, Z. O. Guimarães-Filho, I. L. Caldas, F. A. Marcus, and K. W. Gentle, *Phys. Plasmas* **19**, 012307 (2012).
- ²⁷K. C. Rosalem, M. Roberto, and I. L. Caldas, *Nucl. Fusion* **54**, 064001 (2014).
- ²⁸F. Miskane, X. Garbet, A. Dezairi, and D. Saifaoui, *Phys. Plasmas* **7**, 4197 (2000).
- ²⁹K. C. Rosalem, M. Roberto, and I. L. Caldas, *Phys. Plasmas* **23**, 072504 (2016).
- ³⁰J. H. F. Severo, I. C. Nascimento, Y. K. Kuznetsov, R. M. O. Galvão, Z. O. Guimarães-Filho, F. O. Borges, O. C. Usuriaga, J. I. Elizondo, W. P. De Sá, E. K. Sanada *et al.*, *Nucl. Fusion* **49**, 115026 (2009).
- ³¹C. G. L. Martins, R. E. de Carvalho, I. L. Caldas, and M. Roberto, *J. Phys. A* **44**, 045102 (2010).
- ³²M. S. Santos, M. Mugnaine, J. D. Szezech, A. M. Batista, I. L. Caldas, and R. L. Viana, *Chaos* **29**, 043125 (2019).
- ³³J. D. Szezech, Jr., I. L. Caldas, S. R. Lopes, P. J. Morrison, and R. L. Viana, *Phys. Rev. E* **86**, 036206 (2012).